Materials Chemistry and Physics 143 (2014) 1372–1377

Contents lists available at ScienceDirect

Materials Chemistry and Physics

journal homepage: www.elsevier.com/locate/matchemphys

Copper substitutions in synthetic miargyrite α-$AgSbS_2$ mineral: Synthesis, characterization and dielectrical properties

A. Galdámez [a,*], F. López-Vergara [a], N. Veloso Cid [a], V. Manríquez [a], R.E. Ávila [b]

[a] Departamento de Química, Facultad de Ciencias, Universidad de Chile, Casilla 653, Santiago, Chile
[b] Departamento de Producción y Servicios, Comisión Chilena de Energía Nuclear, Casilla 188-D, Santiago, Chile

HIGHLIGHTS

- $Ag_{0.8}Cu_{0.2}SbS_2$ and $Ag_{0.7}Cu_{0.3}SbS_2$ are isostructural with the natural miargyrite α-$AgSbS_2$ mineral.
- The overall resistance correspond to grain boundary and electrode/sample interface responses.
- In these solid solutions no ferroelectric-like transition is noticed.
- The overall frequency dependence follows the Jonscher's universal power law.
- σ_{ac} vs. frequency can be normalized by Summerfield scaling procedure.

ARTICLE INFO

Article history:
Received 15 October 2012
Received in revised form
24 October 2013
Accepted 24 November 2013

Keywords:
Chalcogenides
Chemical synthesis
Electrical conductivity
Powder diffraction
Dielectric properties

ABSTRACT

The nominal compositions $Ag_{0.8}Cu_{0.2}SbS_2$ and $Ag_{0.7}Cu_{0.3}SbS_2$ have been synthesized by conventional ceramic solid-state reaction at high temperature. X-ray diffraction (XRD) and scanning electron microscopy chemical analysis (SEM-EDAX) revealed single phases, isostructural to the natural miargyrite α-$AgSbS_2$ mineral. Examination of the lattice parameters shows a decrease in the cell volume with increasing copper substitutions. The Raman analysis displays absorptions which may be assigned to the Sb–S stretching vibrations of the SbS_3 pyramids. The impedance-frequency analysis showed grain boundary and electrode interface contributions in non-Debye type relaxation, following Jonscher's universal power law. The giant permittivity response is attributed to extrinsic effects without evidence of a ferroelectric transition. Summerfield scaling, leading to the superposition of impedance analysis, implies that the relaxation is thermally activated, without introducing more than one underlying transport mechanism.

1. Introduction

Research on chalcogenides phases is of great interest because of the promise of ferroelectric, thermoelectric and non-linear optical properties in a non-leaded material. Examples include the compounds $AAsSe_2$ (A = Li, Na) and $AgSbQ_2$ (Q = S, Se) [1–3]. Optical measurement in thin film $AgSbS_2$ point to this material as a good candidate for optical applications [4–6]. On the other hand, Ag_2S–Sb_2S_3 amorphous samples are fast ion conductors and impedance measurements reveal their switching from the predominantly ionic (low frequency) to predominantly electronic conduction (high frequency) over a narrow temperature range [7,8]. An additional modification of the $AgSbS_2$ ternary phase is the preparation of the compounds $(MS)_{1-x}(AgSbS_2)_x$ [9]. These materials are semiconductors with narrow optical gaps in the range from 0.01 to 0.6 eV. Electrical measurement using electronically blocking electrodes (Ag_4RbI_5) in $(MS)_{1-x}(AgSbS_2)_x$ and $AgMSbS_3$, indicated that these phases present ionic or mixed (electronic-ionic) transport *via* silver cations.

The thiopnictides of the type $AgMS_2$ (M = As, Bi or Sb) are sulphosalt minerals that form a complex group of compounds (polymorphs) all of which can be considered in terms of the NaCl-type structure. The polymorph β-$AgSbS_2$ is cubic at high temperature, and it switches to the monoclinic miargyrite (α-$AgSbS_2$) structure, at low temperature [10]. The crystalline structure of the miargyrite natural mineral α-$AgSbS_2$ has been studied by several authors: Hofmann (1938); Knowles (1964) and Smith et al. (1997); however, Effenberger et al. (2002) have shown that miargiryte crystallizes in the C2/c space group, with chains of connected SbS_3

* Corresponding author. Tel.: +56 2 29787267; fax: +56 2 22713888.
E-mail addresses: agaldamez@uchile.cl, acgaldamez1@yahoo.com (A. Galdámez).

0254-0584/$ – see front matter © 2013 Elsevier B.V. All rights reserved.
http://dx.doi.org/10.1016/j.matchemphys.2013.11.048

pyramids [11]. The chains are linked by linear S–Ag–S and AgS_4 polyhedra. The electrical conductivity, σ, in single crystals of α-$AgSbS_2$ and β-$AgSbS_2$ is of the order of 10^{-6} S/m with band-gaps in the range of 1.23–1.73 eV [12]. The relative dielectric permittivity of α-$AgSbS_2$ is $\varepsilon = 12 \pm 0.8$ at a frequency of 100 MHz and temperature of 300 K. This phase shows anomalies in the dielectric permittivity due to the structural transitions of β-$AgSbS_2$ to α-$AgSbS_2$ (in the temperature range of 450–600 K). α-$AgSbS_2$ is a mixed conductor, electronic and ionic *via* silver Ag^+ cations.

An important motivation for this work is the structural and electrical properties due to cationic isoelectric substitutions of Ag^+ (1.28 Å) by Cu^+ (0.98 Å). For this purpose, $Ag_{1-x}Cu_xSbS_2$ ($x = 0.2$ and 0.3) solid solutions were synthesized by solid state reaction, resulting in phases isostructural to the miargyrite α-$AgSbS_2$ natural mineral. The effect of Cu-doping on the dielectric properties was studied by impedance spectroscopy. The two new phases are not ferroelectric but, nevertheless, they show relative dielectric permittivity of $\sim 10^2$ at temperature near ~250 °C.

2. Experimental

All the chemicals in this work were used as obtained: silver(I) sulfide powder, 99.9% purity, Aldrich; antimony(III) sulfide Sb_2S_3 powder, 99.9% purity, Merck; copper(I) sulfide powder, 99.9% purity, Aldrich. All manipulations were carried out under a dry and oxygen-free argon atmosphere. In order to attempt synthesizing single phases with nominal compositions $Ag_{1-x}Cu_xSbS_2$ ($x = 0.2$, 0.3, 0.5, 0.7 and 0.8), a mixture of Ag_2S, Cu_2S and Sb_2S_3 in stoichiometric proportions to give 1–2 g totals, in evacuated quartz ampoules, was gradually heated from room temperature to 850–950 °C in 12 h. The mixture was kept at that temperature for 4 days, followed by cooling to 50 °C at a rate of −12 °C h^{-1}.

The chemical compositions were determined by X-ray energy dispersive analysis (SEM-EDAX) using a JEOL 5400 system equipped with an Oxford LinK ISIS microanalyzer. The X-ray diffraction (XRD) data were collected at room temperature using a Siemens D5000 powder diffractometer, with CuKα radiation in the 5°–80° (2θ) range. The patterns at temperatures ranging from room temperature (RT) to 400 °C were collected using a Panalytical automatic diffractometer X'Pert PROMPD ($CuK\alpha_1 = 1.544426$ Å, $CuK\alpha_2 = 1.54098$ Å), in the range of $5 < 2\theta < 120°$ and step size of 0.0167. The diffractometer is equipped with a heating chamber (Anton Paar HTK1200, PANanalytical BV). The lattice parameters were calculated using the CHECKCELL program. The Raman spectra of the powder samples were recorded in the frequency range of 100–3500 cm^{-1} using a micro-Raman Renishaw 1000 system equipped with Leica-DMLM microscope. The spectra were collected at room temperature with a 633 nm laser line, at a power of 1 mW. Differential scanning calorimetric (DSC) and thermogravimetric analysis (TGA) were performed on a Rheometric Scientific STA 1500H/625 Thermal Analysis System. The DSC/TGA curves were run simultaneously on each sample from room temperature to 1000 °C, in flowing argon at a heating rate of 10 °C min^{-1}. DSC/TGA heating/cooling experiments were conducted in argon atmosphere, from ambient temperature up to ~450 °C (3 cycles). The magnetic measurements were performed on a Quantum Design MPMS XL5 SQUID magnetometer, under a static field of 2.5 kOe and with temperatures increasing from 2 to 300 K.

The electrical properties were studied by impedance spectroscopy and dc methods. Cylindrical pellets, 6 mm in diameter, and ~2 mm thick, were uniaxially pressed for this purpose, at $\sim 5 \times 10^8$ Pa. These were sintered at 400 °C for 48 h in oxygen-free argon atmosphere, resulting in an average pellet density ~90% of the crystallographic density. The two opposite flat surfaces of the pellets were sputtered with platinum and sandwiched between platinum electrodes of the conductivity cell. The dc current–voltage and current–temperature characteristics were measured using a Keithley model 237 source-electrometer. The current–voltage curves were verified to be linear, supporting the ohmic character of the contacts. The impedance measurement was carried out in argon atmosphere using a Solartron Instruments model 1260 analyzer, in the frequency range of 0.1 Hz–10 MHz, with a signal level between 25 mV and 1 V.

3. Results and discussions

3.1. Synthesis, structural and thermal characterization

The homogeneity and chemical compositions of the reaction products were confirmed by SEM-EDAX and XRD. The analysis of the reaction products of nominal stoichiometry $Ag_{1-x}Cu_xSbS_2$ ($x = 0.5$; 0.7 and 0.8) shows compositional inhomogeneities. These samples were obtained with approximately 20% of binary or ternary sulfides impurities. However, homogeneous samples were obtained for the phases with nominal compositions $Ag_{1-x}Cu_xSbS_2$ with $x = 0.2$ and 0.3. The backscattered image and EDAX analysis (chemical maps) revealed that the samples with nominal compositions $Ag_{1-x}Cu_xSbS_2$ ($x = 0.2$ and 0.3) are uniform throughout the scanned region (Fig. 1). These phases are isostructural with the natural mineral miargyrite α-$AgSbS_2$ and the XRD pattern indicated that they are single-phase within the detection limits (Fig. 2). The crystalline structure is formed by chains of corner connected SbS_3 pyramids and $(Ag,Cu)S_4$ tetrahedra. The XRD patterns of the $Ag_{0.8}Cu_{0.2}SbS_2$ and $Ag_{0.7}Cu_{0.3}SbS_2$ were fully indexed in the space group C2/c and the cell parameters are summarized in Table 1. The cell parameters of the solid solutions follow the Vegard's law. The substitution of Ag^+ cations (radius ~1.28 Å) by Cu^+ cations (radius ~0.98 Å) leads to a decrease of the cell volume. The lattice constant values decrease with increasing x (in $Ag_{1-x}Cu_xSbS_2$). The magnetic measurements in $Ag_{0.8}Cu_{0.2}SbS_2$ and $Ag_{0.7}Cu_{0.3}SbS_2$ phases show diamagnetic behavior. Cu^{2+} (d^9) is a paramagnetic cation ($\mu_S = 1.73$ MB), whereas Cu^+ (d^{10}) is a nonmagnetic cation. The magnetic measurements are an experimental evidence of the presence of Cu^+ in these phases.

Fig. 3 shows the Raman spectra recorded at room temperature in several areas of $Ag_{0.8}Cu_{0.2}SbS_2$. The spectra, with main absorptions at ~311, ~279 and ~255 cm^{-1}, are similar throughout the scanned regions. These modes may be assigned to the Sb–S stretching vibrations of SbS_3 pyramids by analogy to $AgSbS_2$ (miargyrite), $TlSbS_2$ (weissbergite) and Sb_2S_3 (stibnite) synthetic minerals [13,14]. The absorption at 194 cm^{-1} may be assigned to the Sb–S bending vibration of SbS_3 pyramids and the absorption at 124 cm^{-1} should correspond to the lattice modes by analogy to Ag_5SbS_4 (stephanite) and Sb_2S_3 (stibnite) minerals [14].

Possible phase transitions were explored by thermal analysis in $Ag_{0.8}Cu_{0.2}SbS_2$ and $Ag_{0.7}Cu_{0.3}SbS_2$ in argon atmosphere. The DSC/TGA analysis, in Fig. 4, shows decomposition at ~500 °C, leading to a gradual mass loss of ~5% at 800 °C. In order to explore the thermal behavior we carried out three DSC-TGA heating–cooling cycles from room temperature to 450 °C. The three DSC heating–cooling cycles are similar. The DSC signal exhibit two peaks, at ~410 °C (heating) and ~435 °C (cooling), which corresponding to incongruent melting point. In the cooling run, the DSC signal shows two exothermic peaks, at ~351 and ~295 °C, which may be attributed to phase transitions or chemical decompositions. DSC/TGA of $Ag_{0.8}Cu_{0.2}SbS_2$ and $Ag_{0.7}Cu_{0.3}SbS_2$ behave similarly. In order to clarify the thermal stability of the samples for electrical measurements, XRD experiments were carried out at various temperatures, from room temperature up to 400 °C (Fig. 2d–f). Cleary,

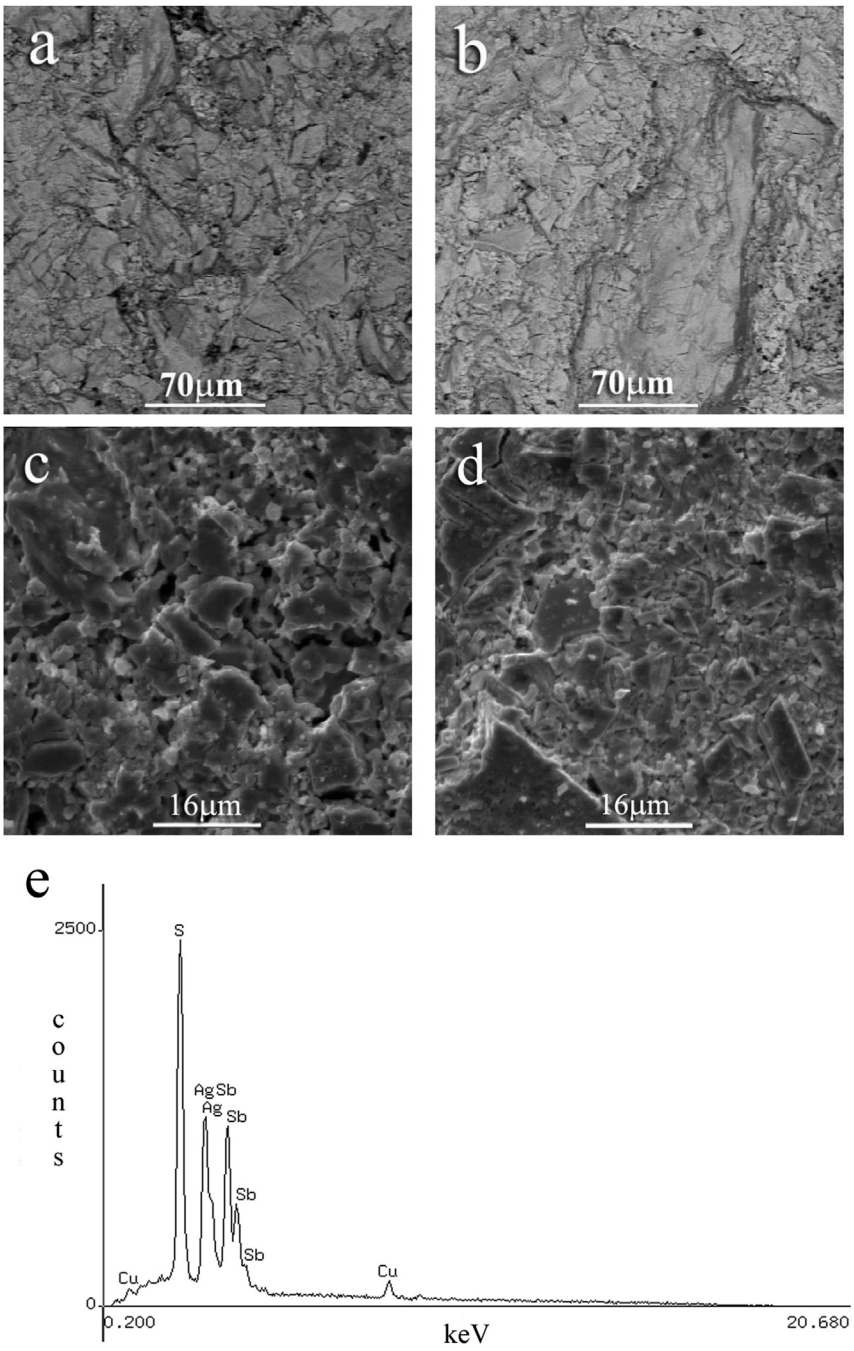

Fig. 1. Scanning electron microscopy (SEM) micrographs: Backscattering electron images of the reactions product of (a) $Ag_{0.7}Cu_{0.3}SbS_2$ and (b) $Ag_{0.8}Cu_{0.2}SbS_2$. Secondary electrons images of sintered pellet of (c) $Ag_{0.7}Cu_{0.3}SbS_2$ and (d) $Ag_{0.8}Cu_{0.2}SbS_2$. An example of EDAX spectral analysis is shown in (e).

aside of some microcrystal growth with heating, no phase changes are evidenced by the XRD patterns, over that temperature range.

Because the melting point of the samples is ~410 °C, pellets for electrical measurements were sintered at ~400 °C by 48 h in oxygen-free argon atmosphere. The sintered pellets show a microstructure consisting of an average grain size of ~8–10 μm with isolated regions of ~17–20 μm grain size (Fig. 1c–d). Some grains show sizes of up to ~30 μm.

3.2. Electrical measurements

The frequency and temperature dependences of the ac conductivity (σ_{ac}) and dielectric permittivity were studied in pellets of $Ag_{0.8}Cu_{0.2}SbS_2$ and $Ag_{0.7}Cu_{0.3}SbS_2$ in the temperature range of room temperature (RT) to 330 °C (frequency range of 0.1 Hz–10 MHz). The impedance–frequency (Z–f) complex plane plots display only one semicircle in the Nyquist plot for temperatures between RT to 210 °C (Fig. 5). Z–f scans over this temperature range were fitted, with the Zview program, assuming one resistor R_1 in series with the parallel combination of a resistor (R_2) and a constant phase element (CPE) of impedance $1/[Y_o(j\omega)\alpha]$, where Y_o is the admittance scale factor, j is the imaginary unit, and ω is the angular frequency. The exponent α assumes values between 0 and 1 [15]. The values of α ~0.7–0.8, clearly below 1, indicate that the charge transport is inhomogeneous with complex network of carrier paths. For $Ag_{0.8}Cu_{0.2}SbS_2$ (temperatures between RT to 210 °C), R_2 decreases

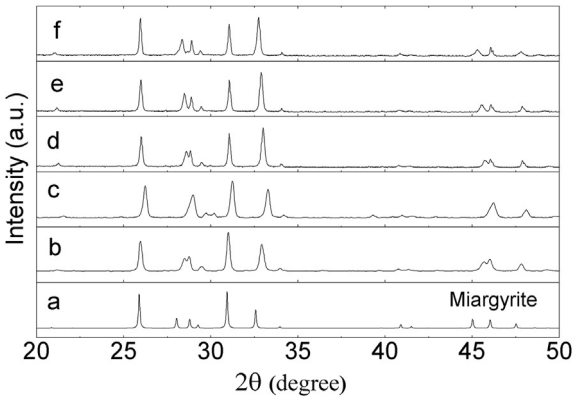

Fig. 2. Powder XRD patterns at room temperature of (a) miargyrite α-$AgSbS_2$ synthetic mineral, (b) $Ag_{0.8}Cu_{0.2}SbS_2$ and (c) $Ag_{0.7}Cu_{0.3}SbS_2$ samples. XRD patterns of $Ag_{0.8}Cu_{0.2}SbS_2$ at various temperatures: (d) 100 °C, (e) 200 °C and (f) 300 °C.

Table 1
Unit cell parameters of the natural miargyrite α-$AgSbS_2$ mineral (single-crystal XRD) and powder samples of $Ag_{0.8}Cu_{0.2}SbS_2$ and $Ag_{0.7}Cu_{0.3}SbS_2$ (PXRD).

Compound	a (Å)	b (Å)	c (Å)	β (°)	V (Å^3)
α-$AgSbS_2$[a]	12.862(3)	4.409(1)	13.218(3)	98.48(2)	741.38(3)
$Ag_{0.8}Cu_{0.2}SbS_2$[b]	12.71(7)	4.43(2)	13.17(7)	99.6(2)	731.2 (3)
$Ag_{0.7}Cu_{0.3}SbS_2$[b]	12.65(9)	4.39(3)	13.19(9)	99.4(4)	722.7(4)

[a] Ref. [11].
[b] This work.

with increasing temperature, with capacitance values of the order of 10^{-12} F, e.g. $\alpha \sim 0.76$, $R_1 \sim 495\ \Omega$ at 100 °C. In the cases of $Ag_{0.7}Cu_{0.3}SbS_2$, $\alpha \sim 0.65$, $R_1 + R_2 \sim 116\ k\Omega$ at 50 °C and $\alpha \sim 0.65$, $R_1 + R_2 \sim 1732\ \Omega$ at 100 °C, and capacitance $\sim 10^{-11}$ F. For temperatures between 210 and 330 °C, the Nyquist plot displays approximately one half of a semicircle, followed by a poorly-resolved, much smaller semicircle (inset Fig. 5). The capacitance value of the first half-semicircle component is of the order of 10^{-12} F.

The dependence of the permittivity on the temperature in $Ag_{0.8}Cu_{0.2}SbS_2$ is shown in Fig. 6. The real part of the relative permittivity was calculated from the relation,

$$\varepsilon'_r(\omega) = \frac{Z''}{\omega \varepsilon_0 G_f |Z|^2} \quad (1)$$

where Z'' is the imaginary part of Z, ω is the angular frequency ($\omega = 2\pi f$), f is the frequency, in Hz and ε_0 is the permittivity of free

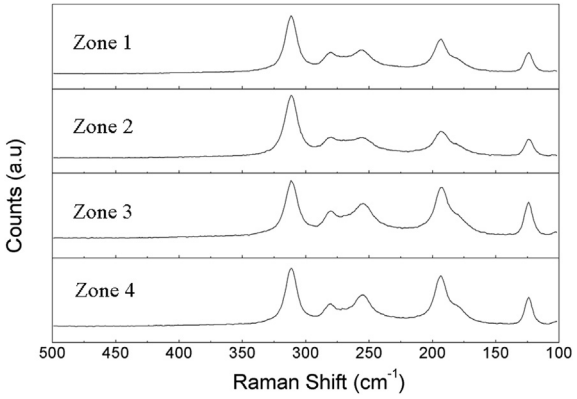

Fig. 3. Raman spectra recorded from several areas of one sample of $Ag_{0.8}Cu_{0.2}SbS_2$ at room temperature.

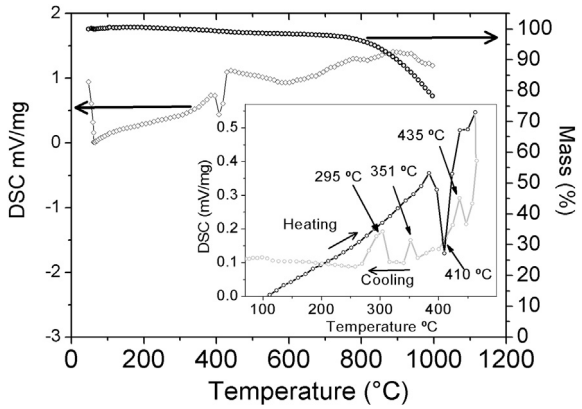

Fig. 4. Thermal analysis, DSC/TGA, of $Ag_{0.7}Cu_{0.3}SbS_2$ from room temperature to 1000 °C. The inset shows DSC heating/cooling cycle from room temperature up to 450 °C in argon atmosphere.

space ($\varepsilon_0 = 8.854 \times 10^{-12}$ F m^{-1}). $G_f = S/d$, where S is the sample area and d is the sample thickness. Two different behaviors are observed in the range of frequency measured. For the first, $\varepsilon'_r \sim 10^5$ and decreases with increasing temperature, over the frequency f range of ~0.1 Hz–90 kHz (Fig. 6). For the second behavior, the ε'_r are below $\sim 10^2$, with slight increase in the frequency range of ~100 kHz to 10 MHz. These values of ε'_r are 10 larger times than those informed in α-$AgSbS_2$ [12]. The permittivity presents a transition at temperature up to ~210 °C for high frequency values (see Fig. 6). However, no ferroelectric-like transition is noticed. This behavior is consistent with the ones previously reported [16,17]. The dielectric permittivity is sharply decreasing vs. angular frequency up to $\omega \sim 10^6$ Hz for $Ag_{0.7}Cu_{0.3}SbS_2$, which is familiarly known as ω^{n-1} variation or non-Debye type behavior (Fig. 7). The low-frequency dispersion of the permittivity may be due to space charge effect, which is produced by the mobility of the ions and the imperfections in the material.

The frequency dependence of the ac conductivity (σ_{ac}) at 60 °C is shown in Fig. 8. The ac conductivity spectrum shows a transition, near $\omega \sim 10^6$ Hz, between the frequency-independent to frequency-dependent regions. The overall frequency dependence follows the Jonscher's universal power law expressions,

$$\sigma_{ac} = \sigma_{dc} + A\omega^n \quad (2)$$

where A is a temperature dependent parameter, ω is $2\pi f$ (frequency f in Hz) and the exponent n represents the degree of interaction of

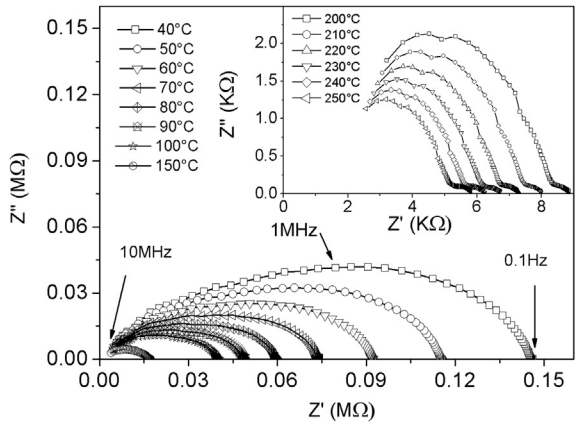

Fig. 5. Impedance–frequency plane plots from $Ag_{0.8}Cu_{0.2}SbS_2$ at various temperatures, in the temperature range of room temperature (RT) to 210 °C. The inset shows impedance–frequency plane plots in the temperature range of 210–350 °C.

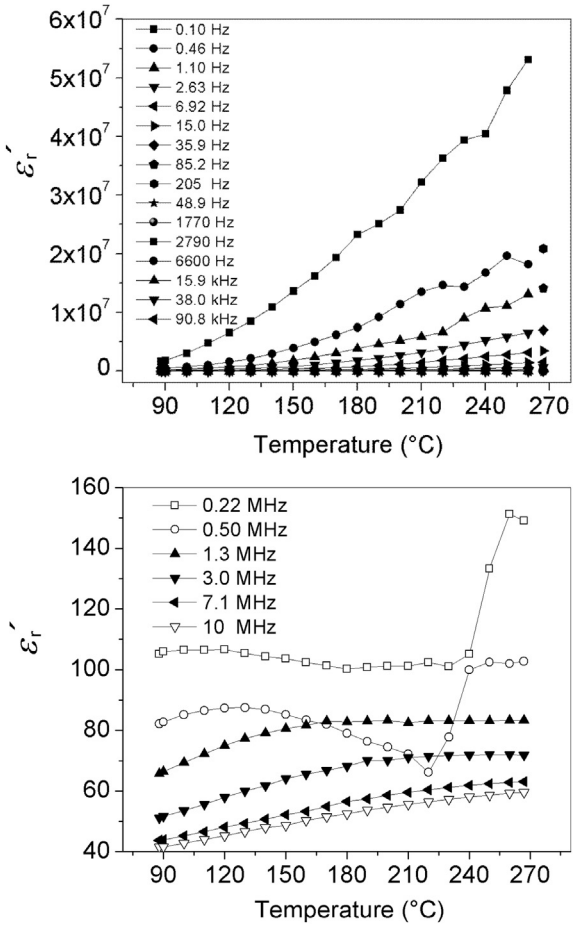

Fig. 6. Real part of the dielectric permittivity vs. temperature from $Ag_{0.8}Cu_{0.2}SbS_2$ (top) in the frequency range of 0.1–90 kHz and (bottom) dielectric real permittivity vs. temperature for high frequency values.

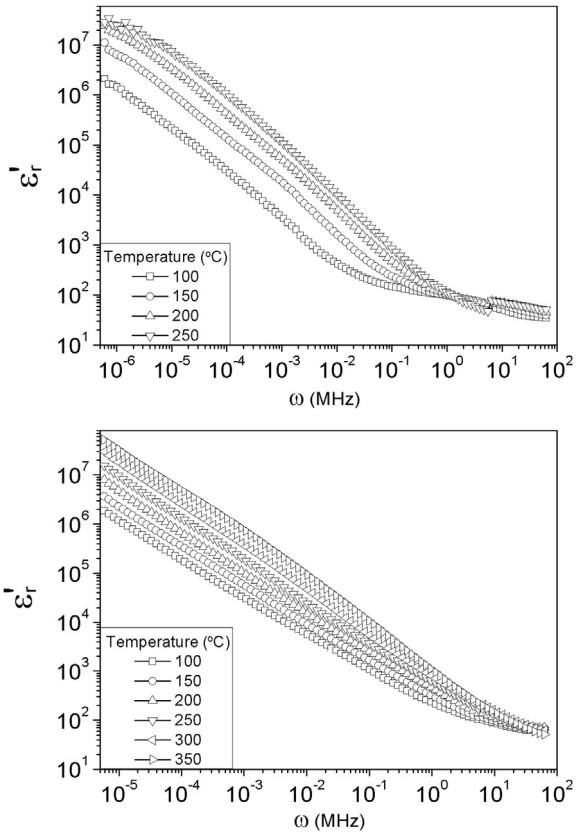

Fig. 7. Dielectric real permittivity vs. frequency of (top) $Ag_{0.8}Cu_{0.2}SbS_2$ and (bottom) $Ag_{0.7}Cu_{0.3}SbS_2$ at various temperatures.

mobile carriers (ions or polarons) with the lattice. The power law was fitted on all curves of $Ag_{0.8}Cu_{0.2}SbS_2$ and $Ag_{0.7}Cu_{0.3}SbS_2$ to evaluate the n exponential constant (see Fig. 8, Table 2). In both samples, the values of n decrease with increasing temperature. West, Funke and Joncher have suggested that the frequency-dependence of the *ac* conductivity reveals important information on the electronic or ion dynamics [18–21]. In addition, Joncher suggests that the exponent $n = (2/\pi)\tan(r)$, r being the ratio of energy loss to energy stored per radian [22]. Silipigni et al. have reported values of $n \sim 0.5$ in $Na_{2-x}Mn_{1-x}PS_3$ (326–350 K) [23]. Besides, electrical measurements reported in single crystal α-,β-$AgSbS_2$ and $(MS)_{1-x}(AgSbS_2)_x$ show that these phases present mixed (electronic–ionic) transport *via* copper or silver cations [9,12]. The n exponent values in $Ag_{0.7}Cu_{0.3}SbS_2$ and $Ag_{0.8}Cu_{0.2}SbS_2$ (see Table 2) may be associated with electronic conductions (hopping polarons) or conduction *via* Ag^+ or Cu^+ cations.

The dc conductivity (σ_{dc}) of the $Ag_{0.7}Cu_{0.3}SbS_2$ and $Ag_{0.8}Cu_{0.2}SbS_2$ phases is thermally activated and obeys the Arrhenius law with activation energy of ~0.2 eV. The current-bias I–V curves are essentially linear. The dc conductivity, σ_{dc}, is approximately 10^{-3} S/m at RT, e.g. $\sigma_{dc} \sim 5.5 \times 10^{-3}$ S m^{-1} at 14 °C in $Ag_{0.7}Cu_{0.3}SbS_2$ and $\sigma_{dc} \sim 1.6 \times 10^{-3}$ S m^{-1} at 17 °C in $Ag_{0.8}Cu_{0.2}SbS_2$. These values are 1000 times larger than those reported in α-$AgSbS_2$ [12]. The spectral shape of the conductivity, σ_{ac} vs. frequency can be normalized by scaling σ_{ac} to σ_{dc} and the frequency axis by the product $\sigma_{dc}T$ [24], according to the following expression,

$$\frac{\sigma_{ac}}{\sigma_{dc}} = F\left(\frac{\omega}{\sigma_{dc}T}\right) \tag{3}$$

where F is a temperature-independent scaling function and ω is $2\pi f$ (f = frequency, in Hz). The Summerfield scaling procedure is shown in Fig. 9 for various temperatures. The first observation is that the plots for all temperatures lead to a master curve, which indicates similarity in the physical mechanics. Marianppan et al. and Galdámez et al. have reported Summerfield scaling in Ca^{2+}-doped $SrBi_2Ta_2O_9$, $PbZr_{0.57}Ti_{0.43}O_3$, $AgPbSb_{1-x}Bi_xS_3$ and $Na_3M_2P_3O_{12}$ orthophosphates crystalline solids [25–27]. These are some examples in which Summerfield scaling applies to systems other than

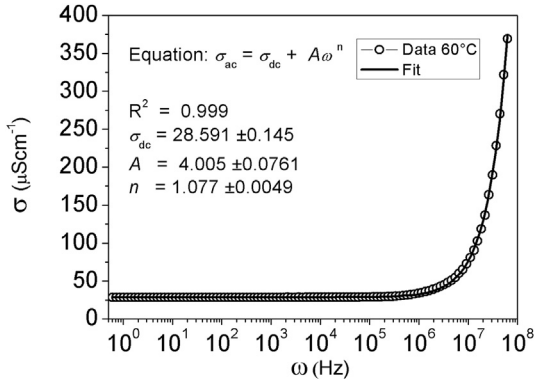

Fig. 8. ac conductivity (σ_{ac}) vs. angular frequency ω at 60 °C of $Ag_{0.7}Cu_{0.3}SbS_2$ showing the non-linear fit to the experimental (Jonsher's) law.

Table 2
Fitting of the spectral shape of σ_{ac} versus frequency at selected temperatures: *dc* conductivity and exponential constant *n* of Jonscher's universal power law.

Temperature (°C)	σ_{dc} (μS cm^{-1})	*n*
$Ag_{0.7}Cu_{0.3}SbS_2$		
100	56.54	0.96
150	125.14	0.81
170	180.48	0.70
200	223.40	0.53
$Ag_{0.8}Cu_{0.2}SbS_2$		
100	74.59	1.10
150	202.02	1.03
200	451.02	0.94
250	832.93	0.63

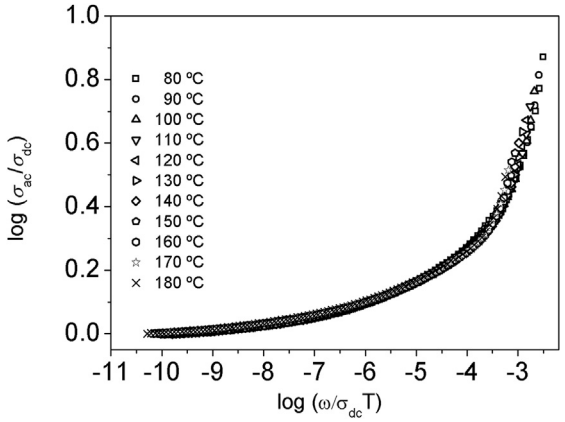

Fig. 9. Master Summerfield scaling curves of $Ag_{0.8}Cu_{0.2}SbS_2$ at various temperatures.

amorphous solids or ionic glasses, as originally considered. The validity of the time–temperature superposition principle (TTPS) in $Ag_{0.7}Cu_{0.3}SbS_2$ and $Ag_{0.8}Cu_{0.2}SbS_2$ implies that the temperature affects the rate of the charge transport efficiency, without introducing more than one underlying transport mechanism.

4. Conclusions

$Ag_{0.7}Cu_{0.3}SbS_2$ and $Ag_{0.8}Cu_{0.2}SbS_2$ were successfully synthesized by ceramic methods at high temperature. SEM-EDAX and powder XRD shows that the samples are homogeneous. The giant permittivity response reported in the literature and reproduced here is attributed to extrinsic effects such as grain boundary and/or sample-electrode interface effects. No ferroelectric-like transition is noticed. The frequency dependence of the imaginary part of the impedance, XRD experiments at different temperatures and the validity of the time–temperature superposition principle (TTPS) implies that the relaxation is thermally activated, without introducing more than one underlying transport mechanism.

Acknowledgments

This work was supported by Fondecyt grant N° 11090153.The authors are grateful to the CAI centers of UCM and Dra. Maria Luisa López for PXRD at variable temperature.

References

[1] T.K. Bera, J.-H. Song, A.J. Freeman, J.I. Jang, J.B. Ketterson, M.G. Kanatzidis, Angew. Chem. Int. Ed. 47 (2008) 7828–7832.
[2] T.K. Bera, J.I. Jang, J.-H. Song, C.D. Malliakas, A.J. Freeman, J.B. Ketterson, M.G. Kanatzidis, J. Am. Chem. Soc. 132 (2010) 3484–3495.
[3] M. Hamam, Y.A. El-Gendy, M.S. Selima, N.H. Teleba, A.M. Salema, Chalcogenide Lett. 6 (2009) 359–365.
[4] J. Gutwirth, T. Wagner, P. Nemec, S.O. Kasap, M. Frumar, J. Non Cryst. Solids 354 (2008) 497–502.
[5] A.M. Ibrahim, J. Phys. Condens. Matter 7 (1995) 5931–5938.
[6] T. Wagner, J. Gutwirth, P. Nemec, M. Frumar, T. Wagner, M. Vlcek, V. Perina, A. Mackova, V. Hnatovitz, Appl. Phys. A 79 (2004) 1561–1562.
[7] J.P. Tiwari, K. Shahi, Ionics 10 (2004) 73–76.
[8] J.P. Tiwari, K. Shahi, Mater. Sci. Eng. B 141 (2007) 8–15.
[9] E.R. Baranovaa, V.L. Kobelev, O.L. Kobeleva, L.L. Nugaeva, V.B. Zlokazov, L.Ya. Kobelev, Solid State Ionics 146 (2002) 415–421.
[10] I. Kelleher, S.A. Redfern, R.A.D. Pattrick, Mineral. Mag. 60 (1996) 393–401.
[11] H. Effenberger, W.H. Paar, D. Topa, A.J. Criddle, M. Fleck, Am. Mineral. 87 (2002) 753–764.
[12] A. Orliukas, V. Valiukenas, V. Kybartas, A. Kezionis, Ferroelectrics 38 (1981) 897–900.
[13] (a) B. Minceva-Sukarova, G. Jovanovski, P. Makreski, B. Soptrajanov, W. Griffith, R. Willis, I. Grzetic, J. Mol. Struct. 651–653 (2003) 181–189.
[14] S. Kharbish, Am. Mineral. 96 (2011) 609–616.
[15] Y. Huang, H. Shih, F. Mansfeld, Mater. Corrosion 61 (2010) 302–305.
[16] T.S. Irvine, D.C. Sinclair, A.R. West, Adv. Mater. 2 (1990) 132–138.
[17] T.B. Adams, D.C. Sinclair, A.R. West, Phys. Rev. B 73 (2006) 094124–094133.
[18] D.P. Almond, A.R. West, Solid State Ionics 9 & 10 (1983) 277–282.
[19] D.P. Almond, C.C. Hunter, A.R. West, J. Mater. Sci. 19 (1984) 3236–3248.
[20] K. Funke, R.D. Banhatti, S. Bruckner, C. Cramer, C. Krieger, A. Mandanici, C. Martiny, I. Ross, Phys. Chem. Chem. Phys. 4 (2002) 3155–3167.
[21] K. Funke, B. Roling, M. Lange, Solid State Ionics 105 (1998) 195–208.
[22] A.K. Jonscher, Nature 267 (1977) 673–679.
[23] L. Silipigni, L. Schiro, L.M. Scolaro, G. De Luca, G. Salvato, Mater. Res. Bull. 47 (2012) 2498–2505.
[24] S. Summerfield, Phil. Mag. B52 (1985) 9–22.
[25] C.R. Mariappan, G. Govindaraj, Physica B 353 (2004) 65–74.
[26] M. Mahesh Kumar, Z.G. Ye, Phys. Rev. B 72 (2005) 024104–024109.
[27] A. Galdámez, F. López-Vergara, P. Barahona, V. Manríquez, R.E. Ávila, J. Solid State Electrochem. 16 (2011) 697–702.